Arbitrary manipulation of amplitude and phase of a set of highly discrete coherent spectra

Masayuki Katsuragawa[1,2,3,*] and Kazumichi Yoshii[1,3,†]

[1]*Department of Engineering Science, University of Electro-Communications, 1-5-1 Chofugaoka, Chofu, Tokyo 182-8585, Japan*

[2]*Institute for Advanced Science, University of Electro-Communications, 1-5-1 Chofugaoka, Chofu, Tokyo 182-8585, Japan*

[3]*Japan Science and Technology Agency, ERATO, Minoshima Intelligent Optical Synthesizer Project, 1-5-1 Chofugaoka, Chofu, Tokyo, Japan*

(Received 17 January 2017; published 31 March 2017)

We describe the attractive optical nature of highly discrete coherent spectra. We show that the relative amplitude and phase of such spectra can be almost arbitrarily manipulated by simply placing three fundamental optical elements—namely, a waveplate, polarizer, and dispersive plate—on an optical axis and then controlling their thicknesses. We also describe the relevant physical mechanism. Furthermore, as a typical application of this optical nature, we demonstrate arbitrary optical waveform generation in a numerical experiment, and we discuss its limitations as an optical-wave manipulation technology and how we can overcome these limitations.

DOI: 10.1103/PhysRevA.95.033846

I. INTRODUCTION

Since the laser was invented in 1960, research efforts to perfectly control optical waves have continued toward the further development of extreme laser technology. Arbitrary optical waveform generation (AOWG)—a typical example of such technology in recent years—was initiated with a picosecond pulsed laser [1] and has now been extended to the femtosecond regime [2,3], which, in another trend, was recently further developed as a line-by-line control scheme [4–9]. Control of carrier-envelope-offset frequency has also flourished in the form of optical frequency combs [10,11] since about 2000, and has now spread further to a variety of extreme optical control technologies, including optical amplitude waveform generation with absolute phase control [9,12] and coherent addition of independent laser radiation over ultrabroad bandwidths [13]. Such innovations in optical wave technology have been applied in practice to a variety of fields, yielding many cross-disciplinary achievements, including quantum state control aimed at manipulation of chemical reactions [14,15]; control of high-order nonlinear optical phenomena such as high harmonic generation (HHG) [16]; and ultrafast attosecond control of dielectric response or electron transport in solids [17,18].

The above-described history indicates the continuing importance of exploring novel possibilities of optical wave control. Here, we describe the attractive optical nature of a set of highly discrete coherent spectra. The relative amplitude and phase of such spectra can be manipulated almost arbitrarily by simply placing a small number of fundamental optical elements on an optical axis and then controlling their thicknesses. Furthermore, as a typical application of this attractive nature, we demonstrate arbitrary waveform generation in a numerical experiment. This optical wave-control technology has a number of advantages, including wide available bandwidth, maintenance of high beam quality, resistance to high-energy laser radiation, and simplicity of optical configuration. It can therefore be utilized for variety of purposes.

II. THEORY

A. Configuration of amplitude and phase manipulations

Figure 1 is a concept diagram of the arbitrary manipulation of amplitude and phase. It is quite simple, consisting of three fundamental optical elements. Here, amplitude and phase are independently controlled: the first two elements—a set comprising a waveplate (a uniaxial birefringent material) and a polarizer—arbitrarily control amplitude, and the last element—a dispersive plate—controls phase. The thickness of the uniaxial birefringent material (waveplate), L_A, the angle of its optical axis from the y axis, θ_A, and also the thickness of the dispersive plate, L_P, are assumed to be precisely adjusted.

What we study here is laser radiation consisting of a set of highly discrete spectra with mutual phase coherence. As a typical example, we discuss optical harmonics consisting of five spectral modes with a frequency spacing of $\Delta\omega = 2\pi \times 124$ THz (124 THz: 2417.68 nm to 620 THz: 483.54 nm) [19]. To make the results more easily understood, we assumed that all the spectral modes of the incident laser radiation were linearly polarized, with an amplitude of unity, a relative phase of zero, and polarization parallel to the y axis in all harmonic modes (Fig. 1). As shown below, these assumptions do not spoil the universality of our discussions.

If the incident laser radiation consists of a single spectral mode (i.e., a single frequency), it is not surprising that amplitude and phase can be arbitrarily controlled by this optical system. What interests us here is that even if the spectra of the incident laser radiation expand broadly, if the spectra are highly discrete, we can still realize almost arbitrary amplitude and phase distributions among the spectral modes by using the same simple optical configuration and its practical control. Further details are given below.

*katsuragawa@uec.ac.jp

†Present address: Department of Physics, Yokohama National University, 79-5 Tokiwadai Hodogaya-ku, Yokohama 240-8501, Japan.

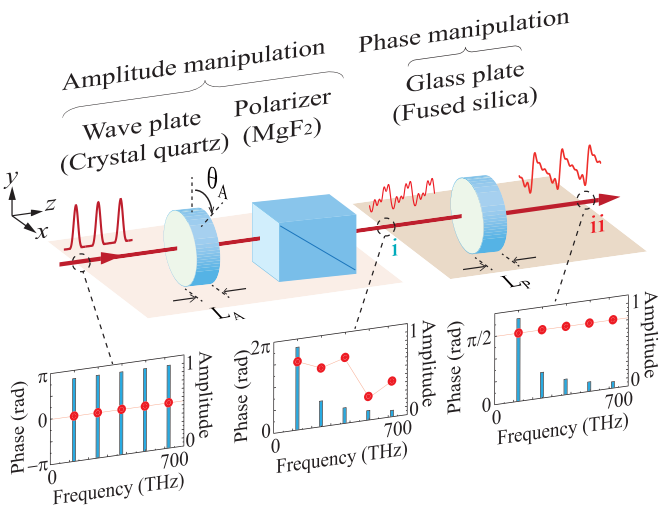

FIG. 1. Schematic illustration of arbitrary amplitude and phase manipulation by using three fundamental optical elements.

B. Physical mechanism of amplitude manipulation

In this optical configuration, the intensity of the electric field of the mth mode transmitted through the polarizer is given by

$$I_m = \left|E_m^y\right|^2 = 1 - \sin^2 2\theta_A \sin^2 \frac{\Gamma_m}{2}, \tag{1}$$

where $\Gamma_m = [n_s(\omega_m) - n_f(\omega_m)]\omega_m \frac{L_A}{c}$. Here n_s, n_f, and $\omega_m(=m\Delta\omega)$, and c are, respectively, the refractive index at the slow axis (optical axis) of the waveplate, the refractive index at the fast axis, the angular frequency at the mth mode, and the speed of light in a vacuum. As seen in this notation, the intensity of the electric field, I_m, of each spectral mode can be manipulated substantially by changing the waveplate thickness L_A and in an auxiliary manner by changing the angle θ_A. To examine in detail the behavior of the electric-field intensity, we conducted calculations by using a quartz crystal plate as the waveplate and a magnesium fluoride (MgF_2) polarizer (57.2 mm long). The refractive indices $n_s(\omega_m)$,$n_f(\omega_m)$ at each harmonic mode were deduced by using the Sellmeier equation [20,21].

Figure 2(a) shows the relationships between the adjacent mode intensities, I_m and I_{m+1} (gray lines), of incident laser radiation consisting of five spectral modes (order: m = 1, 2, 3, 4, 5). We fixed θ_A at $\pi/4$ and varied the thickness of the waveplate L_A from 10 to 12 mm. In this expression, the intensity relationship I_m-I_{m+1} draws a Lissajous curve; the frequency ratio characterizing this trajectory is given by

$$\frac{\Gamma_{m+1}}{\Gamma_m} = \frac{\Delta n_{m+1}}{\Delta n_m}\frac{m+1}{m}, \tag{2}$$

where $\Delta n_m = n_s(\omega_m) - n_f(\omega_m)$. The term $\frac{\Delta n_{m+1}}{\Delta n_m}$ on the right-hand side is usually close to unity; in other words, the frequency ratio of the Lissajous trajectory, $\frac{\Gamma_{m+1}}{\Gamma_m}$, is characterized substantially by the mode ratio, $m+1:m$. When the laser radiation consists of a highly discrete spectrum, m is a small integer, and this causes the Lissajous trajectories to fairly differ in shape between the different combinations of modes [Fig. 2(a)]. As a result, a variety of intensity distributions among the spectral modes are generated. In other words, as the intensity I_m of the transmitted laser is a periodic function of the thickness, L_A, the periods will vary greatly among the spectral modes if the modes are highly discrete: a variety of intensity distributions are thus generated. Looking at the term $\frac{\Gamma_{m+1}}{\Gamma_m}$ in more detail, we notice another important point, namely that $\frac{\Delta n_{m+1}[(m+1)\Delta\omega]}{\Delta n_m(m\Delta\omega)}$ deviates from unity by a non-negligible amount in the order of 10^{-2}. As drawn in Fig. 2(a), the relative intensity space $\{I_m, I_{m+1}\}$ is thereby densely filled with Lissajous trajectories with relatively few cycles from 10 to 100 s. The large degree of discreteness of the spectra makes this non-negligible deviation from a complete periodic cycle of the Lissajous trajectories. One hundred cycles correspond to a change in waveplate thickness, L_A, of a few tens of millimeters, at most. The above two mechanisms enable us to practically generate arbitrary amplitude distributions among the spectral modes.

Here, we give an example of arbitrary amplitude manipulation in which, as a target, we explore the intensity distribution required to generate a sawtooth waveform in the time domain, i.e., $\{I_1 = 1, I_2 = 1/4, I_3 = 1/9, I_4 = 1/16, I_5 = 1/25\}$ for five spectral modes. By setting this intensity distribution as a target, we explored the optimal waveplate thickness, L_A, and the optimal angle from the optical axis, θ_A. We used the random search method [22], a numerical optimization method, to explore the optimal solution. Here, we defined a deviation from the target as $\sum_{m=2}^{5} {\delta_m}^2$; we set this as the objective function and minimized it, whereby

$$\delta_m = \left(I_m^0 - \frac{I_m(L_A,\theta_A)}{I_1(L_A,\theta_A)}\right) \Big/ I_m^0 \tag{3}$$

and I_m^0 is the target intensity at the mth mode.

Exploration revealed a spectral intensity distribution closest to the target at $L_A = 11.447$ mm ($\theta_A = \pi/4$). We mark this point with a star in Fig. 2(a). We also indicated the trajectory (blue lines and arrows) corresponding to a 120-μm-thickness change in L_A before it reached this optimal solution. The red lines in Fig. 2(a) indicate the desired intensity ratios between adjacent modes. The dark-green-shaded areas show the range of values within $\pm 10\%$ of the exact target, and the light-green-shaded areas cover values within $\pm 20\%$. After many quasicyclic Lissajous motions with fairly different respective frequencies, all the relative intensity distributions among the five modes simultaneously came close to the target at $L_A = 11.447$ mm.

In this example of arbitrary amplitude manipulation, all the mode intensities of the incident laser radiation were assumed to be unity. However, it can be understood by the results shown in Fig. 2(a) that this amplitude manipulation is not dependent on the initial mode-intensity distributions.

Generally, refractive-index dispersion increases as wavelength becomes shorter, whereas its anisotropy, $n_s - n_f$, conversely tends to become smaller as the wavelength shortens. As we have stated above, the non-negligible deviation of $\frac{\Delta n_{m+1}}{\Delta n_m}$ from unity plays an important role in generating a variety of intensity distributions. Therefore, this amplitude-manipulation technology gradually becomes impractical as the relevant spectra span shorter wavelengths.

C. The physical mechanism of phase manipulation

Next, we describe the phase manipulation in detail. Because our present set of discrete spectra consists of five spectral

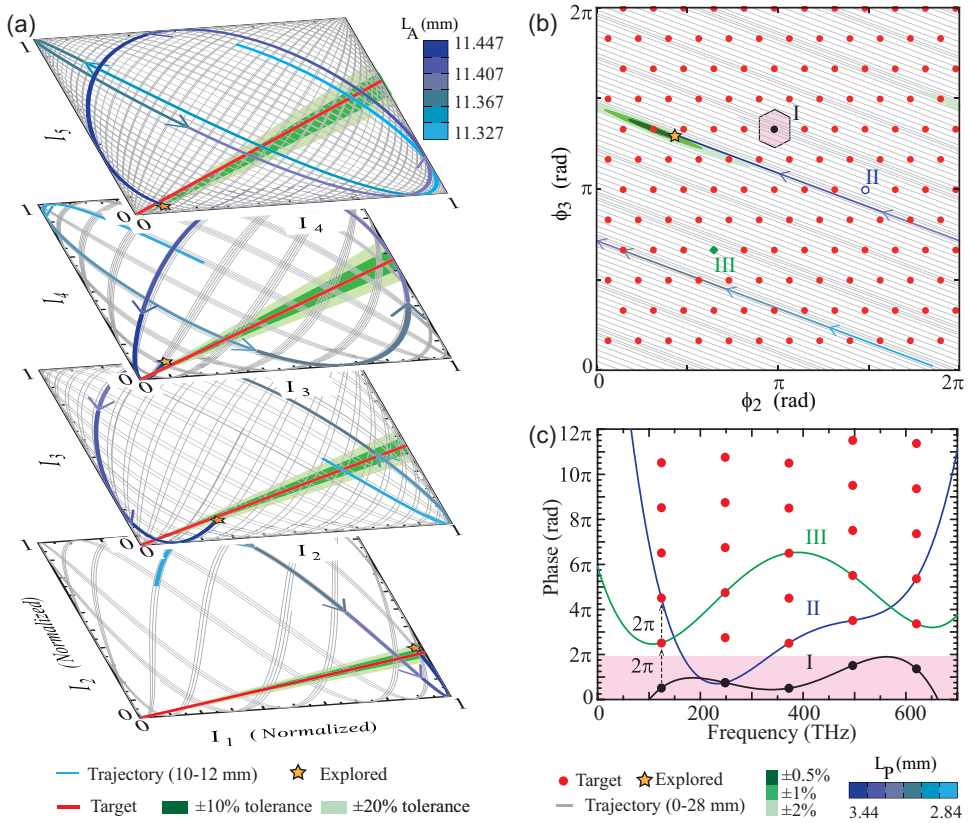

FIG. 2. Physical mechanism of amplitude and phase manipulation. (a) Parametric plots (gray lines) of normalized spectral mode intensities as a function of waveplate thickness, L_A. Target relative intensities are shown as red lines. The star marks the explored optimal possible solution. (b) Dispersion coefficients ϕ_2 and ϕ_3; the coefficient corresponding to the target spectral phase is shown as the black dot and other, equivalent, coefficients are indicated by red dots. (c) Target spectral phase (black dots) and its equivalent spectral phases (red dots).

modes, the relative spectral phase among them can, in principle, be represented using up to fourth-order dispersions:

$$\phi(\omega_m) = \sum_{k=2}^{4} \{\Phi_k L_P (m\Delta\omega)^k\}. \tag{4}$$

Here, the zero and first-order terms are not included and we use the remaining terms of second order or higher, as our main concern is the manipulation of dispersion. In addition, because phase is a periodic function of 2π, each dispersion-order term, excluding the integer, m^k, is replaced as follows:

$$\phi_k = \mathrm{mod}[\Phi_k L_P \Delta\omega^k, 2\pi]. \tag{5}$$

Using this notation, the spectral phase is written in brief as

$$\phi'(\omega_m) = \phi_2 m^2 + \phi_3 m^3 + \phi_4 m^4. \tag{6}$$

To gain a detailed understanding of this spectral phase behavior, we performed a numerical calculation using a fused silica plate as a dispersive material [23]. We varied the thickness of the fused silica plate, L_P, from 0 to 28 mm, and studied the behavior of each order term of the dispersion.

Figure 2(b) plots the relationship between the second- and third-order dispersions,ϕ_2 and ϕ_3 (gray lines). As the spectra were highly discrete ($\Delta\omega$: $2\pi\times124$ THz), these dispersion terms included large coefficients ($\Phi_2\Delta\omega^2 = -1.786\times10^1$ rad/mm, $\Phi_3\Delta\omega^3 = 6.664$ rad/mm), despite the high order dispersion terms. As a result, the entire (ϕ_2, ϕ_3) space was almost filled in response to an L_P thickness change of less than 30 mm. The fourth-order dispersion also had a large coefficient, $\Phi_4\Delta\omega^4 = -4.602\times10^{-1}$ rad/mm; consequently, the entire (ϕ_3,ϕ_4) space was filled simultaneously.

Qualitatively, the physical mechanism of phase manipulation is similar to that of the amplitude manipulation. As the spectra are highly discrete, each order term of the dispersions independently and considerably varies upon a small change in thickness of the dispersive element, resulting in a variety of combinations among the high-order dispersions. It produces almost arbitrary spectral phases, although we only manipulate the thickness of a single dispersive plate.

As an example of this spectral-phase manipulation, Figure 2(b) shows the results obtained when we explored Spectral Phase I—i.e., the optimum solution marked with a star ($\phi_2 = 0.9847$ rad; $\phi_3 = 4.176$ rad) and the trajectory (dark blue line) over 600 μm toward its solution ($L_p = 3.4396$ mm). Here Spectral Phase I is the addition of spectral phase to generate a sawtooth wave in the time domain when the spectral phase at position i in Fig. 1 is set as the starting point. Looking only at this solution space (ϕ_2,ϕ_3) of Fig. 2(b), there appears to be a better one. However, as a solution to achieve Spectral Phase I which includes the fourth-order dispersion, ϕ_4, this star point gave the optimal result within the present exploration range.

By the way, if we perform numerical calculations in this way, we notice an interesting fact. Surprisingly, we find that

solutions almost comparable to the optimal one [marked with a star in Fig. 2(b)] appear much more frequently than expected. Hereinafter, we describe this specific property of phase manipulation: namely, the physical mechanism behind the appearance of so many near-optimal solutions.

The main reason is that, because phase is a periodic function of 2π, there is an infinite number of spectral phases equivalent to the target spectral phase. Taking Spectral Phase I (p_m, phase at spectral mode m, $0 \leqslant p_m < 2\pi$) in Fig. 2(c) as an example, the target spectral phase p_m is located at an interval of 2π at each spectral mode and forms an overall lattice pattern [red dots in Fig. 2(c)]. Regardless of which lattice points are selected at each spectral mode, all of the spectral phases are equivalent to each other; whereas the dispersions involved in the spectral phases vary according to which lattice points are selected.

As examples, in Fig. 2(c) we show Spectral Phases II and III in addition to I. The coefficient of each order term of the dispersions comprising these spectral phases can be determined exactly by solving the set of the following equations, which hold at each spectral mode:

$$p_m + 2q_m\pi = \sum_{k=0}^{4} \Phi_k L_p (m\Delta\omega)^k, \tag{7}$$

where q_m is an integer. I, II, and III in Fig. 2(b) are plots of the dispersions obtained in this way, where the dispersions have been converted as $\phi_k = \mathrm{mod}[\Phi_k L_P \Delta\omega^k, 2\pi]$. Conducting the same solving process for all of the other combinations with the lattice points in Fig. 2(b) as well reveals that the dispersion coefficients comprising the target phase p_m also make a lattice pattern in the solution (dispersion term) space, as shown in red in Fig. 2(b).

The second-order dispersion ϕ_2 is eventually reduced to the following 24 solutions, 4!:

$$\phi_2 = 2\pi\frac{s}{24} + \frac{P_2}{24} \quad (s = 0,1,\ldots,23). \tag{8}$$

Similarly, the third-order dispersion ϕ_3 is reduced to $12 = 4!/2$ solutions. Consequently, in the entire (ϕ_2, ϕ_3) space, $144 = (24\times12)/2$ solutions are formed, in a lattice pattern (see the Appendix). Because the lattice points represent an equivalent spectral phase, eventually the solution space to be explored is dramatically reduced, by approximately two orders, from the entire $2\pi\times2\pi$ space to the hexagonal area illustrated in Fig. 2(b).

This relationship between the spectral-phase space [Fig. 2(c)] and the solution space with the dispersions [Fig. 2(b)] is analogous to the lattice-reciprocal lattice (Brillouin zone) relationship in a solid, although here the bases are polynomial functions.

The other reason that near-optimal solutions are so frequently found is that the allowable error around the exact solution is very large. If we allow a slight error in the target spectral phase, a similar amount of error relative to the entire phase area of $2\pi^3$ is allowed in the solution space with dispersions. However, the solution space is effectively reduced [to the hexagonal area in Fig. 2(b)] by the number of lattice points, as described above; thereby, conversely, the allowable error is effectively magnified by the same number of lattice points. As an example, in Fig. 2(b) we show the near-optimal solution areas, in three shades of green, in cases in which an error of $\pm0.5\%$, $\pm1\%$, or $\pm2\%$ can be allowed for the target phase p_m. If an error of at most 2% is allowed around the target spectral phase, a cigar-shaped area that is fairly large relative to the hexagonal unit-cell solution space is allowed as a near-optimal solution.

Here, if we again go back to the discussion of the result of exploring the target Spectral Phase I, we find that the optimal solution [marked with a star in Fig. 2(b)] obtained is not near the exact solution I, but is in fact located close to another equivalent lattice solution-point including the allowable error area. It turns out that the mechanism by which the exploration range could be effectively reduced to the unit-cell solution space, and conversely, the fact that the allowable error could be effectively enlarged was of benefit in the exploration of solutions.

At the end of this discussion we note some more points regarding phase manipulation.

If a different spectral phase, p_m, is specified as a target, all of the lattice-pattern solutions in Fig. 2(b) shift translationally. Thus the possibility of finding near-optimal solutions does not depend on either the initial or the target spectral phases.

The trajectory of the dispersions in the solution space as a function of the dispersive-plate thickness L_P is a property intrinsic to the dispersive material. On the other hand, the shape of the allowable error around the exact solution for the target spectral phase is formed independently of such intrinsic properties. When the allowable error is cigar shaped and the orientation of its longitudinal axis is close to the trajectory, as represented in Fig. 2(b), control of the spectral phases becomes robust against plate thickness adjustment.

As the number of spectral modes increases, the number of lattice points in the solution space increases accordingly as (mode number -1)!. However, at the same time, the mode-number increment causes the increase in the dispersion orders to be controlled. Furthermore, the dispersion term ϕ_k becomes smaller as the order becomes higher; i.e., the dispersive plate thickness required to fill the solution space of the dispersions increases. Therefore, overall, it becomes gradually more difficult to find the target spectral phase as the number of spectral modes increases.

The number of lattice points in the solution space does not depend on the frequency spacing of the spectral modes, $\Delta\omega$. However, this does not mean that our phase manipulation is independent of the mode spacing $\Delta\omega$ (i.e., of discreteness in the spectra). If $\Delta\omega$ becomes smaller, although the lattice structure itself does not change, the trajectory created as a function of the dispersive-plate thickness L_P is traced closer to the edges of the solution space. This makes it difficult to reach the target spectral phase. Incidentally, if the mode spacing is $\Delta\omega = 2\pi\times10$ THz—one digit smaller than in Fig. 1 [24,25]—the second-order dispersion, $\Phi_2\Delta\omega^2$, is of the order of 10^{-2}; the third-order dispersion, $\Phi_3\Delta\omega^3$, is of the order of 10^{-3}; and the fourth-order dispersion, $\Phi_4\Delta\omega^4$, is of the order of 10^{-6}. In short, a thickness adjustment of more than a few hundred meters is required to fill the entire solution space, so the technology becomes impractical.

One might suppose that this spectral-phase manipulation is similar to that of the TT method [26]. In fact, from one

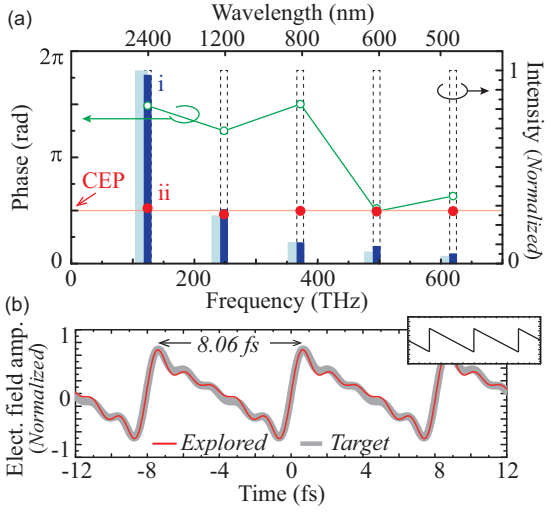

FIG. 3. Synthesis of a sawtooth electric waveform as a typical example of spectral amplitude and phase manipulations. (a) Target (light blue bars) and achieved (dark blue bars) intensity distributions and spectral phases before (green circles) and after (red dots) phase manipulation. (b) Target (gray) and synthesized (red) electric-field waveforms. Inset shows an ideal sawtooth waveform.

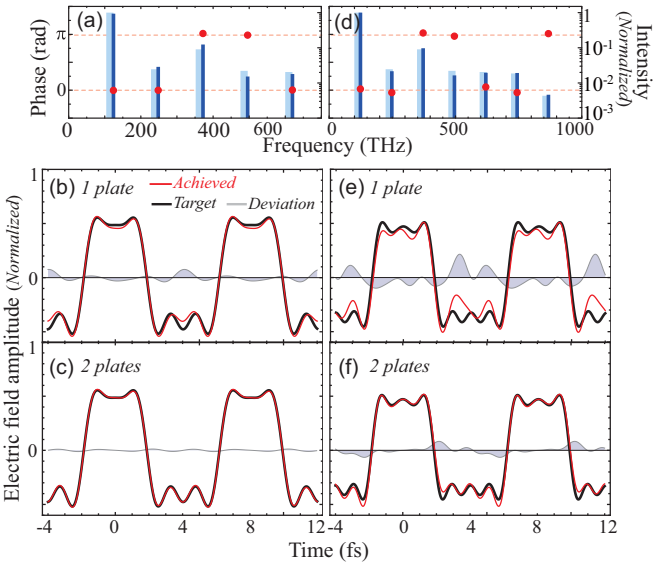

FIG. 4. Application to arbitrary optical waveform generation. The target is a square waveform (duty ratio, 45:55). Intensity distributions (light blue bars, target; dark blue bars, achieved), spectral phases (red dots), and electric-field waveforms (black curves, target; red curves, achieved; gray shading, deviations from target) are shown for a, b, and c (five spectral modes) and for d, e, and f (seven spectral modes).

perspective our method can involve TT: namely, the solution corresponding to the high-order TT [27,28] appears at an interval of 2π in the solution space in Fig. 2(b). Also, high-order TT requires different dispersive materials, the number of which is equal to the order number of the dispersions to be considered, because the respective terms of the dispersions are precisely controlled. In reality, it is difficult to find such exact solutions. TT, including high-order TT, is conceptually different from the concept presented here [27,28].

III. APPLICATION TO ARBITRARY OPTICAL WAVEFORM GENERATION

Last, we describe the application of this optical nature of highly discrete spectra to AOWG. By using AOWG as a typical example, we also discuss the limitations of this optical wave-control technology and ways of overcoming these limitations.

The electric-field waveform, $E(t)$, formed by the five spectral modes in the time domain is given simply by

$$E(t) = \sum_{m=1}^{5} a(\omega_m) \exp[i\{\omega_m t - \phi(\omega_m)\}], \qquad (9)$$

where $a(\omega_m)$ is the amplitude at the mth mode. The absolute phase or carrier-envelope phase (CEP), which is not shown explicitly in this equation, is assumed to be stable [9,19].

The both examples of arbitrary amplitude and phase manipulations, demonstrated in Figs. 2(a) and 2(b), were the amplitude distributions and spectral phases required to generate a sawtooth wave in the time domain. In Fig. 3(a), we show again the results obtained. The light and dark blue bars are the target and achieved intensity distributions, respectively. The green circles and solid red circles are, respectively, the initial (position i in Fig. 1 was set as the starting point) and achieved spectral phases. The red curve in Fig. 3(b) is the electric-field waveform retrieved in the time domain using the intensity distributions and spectral phases shown in Fig. 3(a). The electric-field waveform achieved was in good agreement (correlation coefficient [29]: 0.9956) with the target sawtooth wave (gray line) with a repetition period of 8.06 fs, which was constructed using the ideal intensity distribution $\{I_1 = 1, I_2 = 1/4, I_3 = 1/9, I_4 = 1/16, I_5 = 1/25\}$ and spectral phases ($p_1 = \pi/2, p_2 = \pi/2,\ p_3 = \pi/2,\ p_4 = \pi/2,\ p_5 = \pi/2$) to achieve the target.

Strictly speaking, control of field-amplitude waveforms requires control of the absolute phase. However, the absolute phase can be controlled with a much smaller change in dispersive-plate thickness compared than that required in the relative spectral-phase case. Therefore, we can achieve full absolute-phase control of 0 to 2π simultaneously with the relative-phase control by adding a slight amount of dispersive-plate-thickness control within an allowance at $L_p(\sim\pm\mu\text{m})$, which does not disturb the optimal solution obtained for the relative spectral phase. It is also possible to control the absolute phase independently in the generation process of a set of discrete spectra [9,19]. Here, for the purposes of our discussion, we assumed that the absolute phase was controlled to $\pi/2$.

The technology described here can be applied to any waveform, including to sawtooth waves. Figure 4 is another example of AOWG, in which a rectangular wave with a duty ratio of 45:55 is set as the target waveform. The ideal intensities and phases of this rectangular wave are $(1, 2.45\times10^{-2},\ 9.04\times10^{-2},\ 2.21\times10^{-2},\ 2.05\times10^{-2})$ and $(0, 0, \pi, \pi, 0)$, respectively.

The optimal solution was obtained when the thickness L_A and angle θ_A of the amplitude-control element were set to 8.192 mm and 42.22°, respectively, and the thickness

L_P of the phase-control element was set to 28.355 mm. Figure 4(a) shows the intensity distributions and spectral phases obtained, and Figure 4(b) shows the electric-field waveform (the red line) composed of these intensities and phases. The gray areas indicate the residual deviation from the target electric-field waveform (the black line). The electric-field waveform generated is in very good accord with the target (correlation coefficient: 0.9980). Here, the CEP was assumed to be adjusted to 0 at position ii in Fig. 1 in the process of generating a set of discrete spectra [9,19].

If we increase the number of spectral modes, although on the other hand, such an increase in number of spectral modes to be simultaneously controlled makes it difficult to explore the optimal solution, the electric-field waveform can be made closer to the ideal shape. Figures 4(d) and 4(e) show the results when the spectral modes were increased from five to seven components. The optimal solution was obtained when the amplitude-control elements were set to $L_A = 12.695$ mm and $\theta_A = 45.00^\circ$, respectively, and the phase-control element was set to $L_P = 33.022$ mm. As seen in these figures, the electric-field waveform more closely approached an ideal rectangular shape, but accordance with the target was degraded (correlation coefficient: 0.9820), because of the increase in number of spectral modes to be controlled.

As easily imagined, we can achieve more accurate control for more spectral modes by increasing the species of materials to provide greater variability in amplitude and phase control. If we explain this mechanism using Fig. 2, it means that solutions are explored with more freedom such that different trajectories provided by different materials can be superimposed on arbitrary weights. Figure 4(f) shows the results when a plate made from MgF_2 (a uniaxial birefringent material) was employed as a waveplate for amplitude control in addition to the quartz plate. The optimal solution was obtained when the quartz and MgF_2 plates were set to $L_A = 1.657$ mm, $\theta_A = 38.41^\circ$ and $L_A = 14.009$ mm, $\theta_A = 43.22^\circ$, respectively, and when the phase-control element was adjusted to $L_P = 36.997$ mm. The practicality of the technology is partially reduced, but, instead, the agreement between waveform and target is greatly improved (correlation coefficient: 0.9965). For reference, if we apply this extended method to the five spectral modes, as shown in Fig. 4(c) we obtain an electric-field waveform that perfectly matches the target (correlation coefficient: 0.9999). Here, the thickness L_A and angle θ_A of the quartz plate were 8.913 mm and 43.94°, respectively; the thickness L_A and angle θ_A of the MgF_2 plate were 5.642 mm and 23.11°, respectively; and the thickness L_P of the phase control plate was 12.903 mm.

Finally, some brief comments. When a waveform has an inversion symmetry of, for example, a rectangular or triangular shape, with a duty ratio of 50:50, the target amplitude distribution includes zero spectral-amplitude modes. In this case, it is difficult to obtain good accordance with the target waveforms if amplitude control is attempted by using only a single waveplate material. An extended approach employing more than two waveplate materials, as described above, is required.

In this study, we have not yet discussed spectral width or pulsed duration of the incident laser radiation. The present optical technology can be applied within certain limits, even if the incident optical wave is short-pulsed laser radiation. The limitation on application of this technology is chiefly determined by the group velocity walk-off of the incident pulsed laser radiation. For instance, if the relevant bandwidth spans 480 nm to 2.4 μm with five spectral modes, the maximal group velocity walk-off is estimated to be 60 fs/mm for a fused silica glass plate. As a result, one criterion for appropriately applying this optical technology is that the pulsed duration of the incident radiation is longer than several tens of picoseconds.

IV. CONCLUSIONS

We have described the attractive optical nature of a set of highly discrete spectra. We showed that the relative amplitude and phase among such spectra could be almost arbitrarily manipulated by simply placing three fundamental optical elements (a waveplate, a polarizer, and a dispersive plate) on an optical axis and controlling their thicknesses. Furthermore, we showed that the thicknesses required to satisfy these requirements could be found frequently; that is, this spectral characteristic was applicable as a practical optical technology. We also revealed the physical mechanism behind the technology. Moreover, as an example of the practical application of the technology, we demonstrated arbitrary optical waveform generation in a numerical experiment in which a sawtooth or rectangular wave was set as a target. Finally, we discussed the limitations of this optical technology and how to overcome them. The idea described here can be extended to polarization control [30] too, such as the targeting of vector waveform generation [31]. This will be discussed elsewhere.

This technology does not require the spatial separation of each spectral mode. Therefore, it maintains high beam quality and is robust against disturbances in the same way as the common mode in electronics. The technology also uses only optical elements with a high damage threshold. We can apply this technology to Joule-class high-energy laser beams. The following would be attractive potential applications of this optical technology: generation of a train of high-power (∼GW) monocycle pulses at repetition rates above 100 THz [28,32] by manipulating high-order stimulated Raman scattering radiation [33–37]; generation of single-frequency soft x rays using a monocycle pulse train as a driving laser for HHG processes; and ultrafast optical switching based on the electric current or dielectric polarization response induced in a dielectric material using a 100-THz ultrafast pulse train [17,18]. Future research challenges include electron motion control with arbitrary optical waveforms [38,39] and control of nonlinear wavelength conversion by implementing arbitrary relative-phase manipulation in a nonlinear optical process [40].

APPENDIX: PROPERTY OF SOLUTION SPACE MADE BY DISPERSIONS INCLUDED IN THE SPECTRAL PHASE

We assume that the Five Modes Spectral Phase noted as I in Fig. 2(c) are $\phi(\omega_m) = (p_1, p_2, p_3, p_4, p_5)$, $0 \leqslant p_m \leqslant 2\pi$. Considering degree of freedom of 2π in phase, the dispersions included in the spectral phase are given as solutions for the

following set of five equations:

$$\begin{aligned}
\psi_0 + \psi_1\Delta\omega + \psi_2\Delta\omega^2 + \psi_3\Delta\omega^3 + \psi_4\Delta\omega^4 &= p_1 + 2q_1\pi,\\
\psi_0 + \psi_1 2\Delta\omega + \psi_2(2\Delta\omega)^2 + \psi_3(2\Delta\omega)^3 + \psi_4(2\Delta\omega)^4 &= p_2 + 2q_2\pi,\\
\psi_0 + \psi_1 3\Delta\omega + \psi_2(3\Delta\omega)^2 + \psi_3(3\Delta\omega)^3 + \psi_4(3\Delta\omega)^4 &= p_3 + 2q_3\pi,\\
\psi_0 + \psi_1 4\Delta\omega + \psi_2(4\Delta\omega)^2 + \psi_3(4\Delta\omega)^3 + \psi_4(4\Delta\omega)^4 &= p_4 + 2q_4\pi,\\
\psi_0 + \psi_1 5\Delta\omega + \psi_2(5\Delta\omega)^2 + \psi_3(5\Delta\omega)^3 + \psi_4(5\Delta\omega)^4 &= p_5 + 2q_5\pi,
\end{aligned} \tag{A1}$$

where q_m is an integer. To simplify the notation, the spectral phase is rewritten as $\phi(\omega_m) = \sum_{k=0}^{4}\{\Phi_k L_P (m\Delta\omega)^k\} = \sum_{k=0}^{4}\{\Psi_k (m\Delta\omega)^k\}$. Solving this set of equations for ψ_k, we obtain

$$\begin{pmatrix} 1 & \Delta\omega & \Delta\omega^2 & \Delta\omega^3 & \Delta\omega^4 \\ 1 & 2\Delta\omega & (2\Delta\omega)^2 & (2\Delta\omega)^3 & (2\Delta\omega)^4 \\ 1 & 3\Delta\omega & (3\Delta\omega)^2 & (3\Delta\omega)^3 & (3\Delta\omega)^4 \\ 1 & 4\Delta\omega & (4\Delta\omega)^2 & (4\Delta\omega)^3 & (4\Delta\omega)^4 \\ 1 & 5\Delta\omega & (5\Delta\omega)^2 & (5\Delta\omega)^3 & (5\Delta\omega)^4 \end{pmatrix} \begin{pmatrix} \psi_0 \\ \psi_1 \\ \psi_2 \\ \psi_3 \\ \psi_4 \end{pmatrix} = \begin{pmatrix} p_1 + 2q_1\pi \\ p_2 + 2q_2\pi \\ p_3 + 2q_3\pi \\ p_4 + 2q_4\pi \\ p_5 + 2q_5\pi \end{pmatrix}, \tag{A2a}$$

$$\begin{aligned}
\begin{pmatrix} \psi_0 \\ \psi_1 \\ \psi_2 \\ \psi_3 \\ \psi_4 \end{pmatrix} &= \begin{pmatrix} 5 & -10 & 10 & -5 & 1 \\ -\frac{77}{12\Delta\omega} & \frac{107}{6\Delta\omega} & -\frac{39}{2\Delta\omega} & \frac{61}{6\Delta\omega} & -\frac{25}{12\Delta\omega} \\ \frac{71}{24\Delta\omega^2} & -\frac{59}{6\Delta\omega^2} & \frac{49}{4\Delta\omega^2} & -\frac{41}{6\Delta\omega^2} & \frac{35}{24\Delta\omega^2} \\ -\frac{7}{12\Delta\omega^3} & \frac{13}{6\Delta\omega^3} & -\frac{3}{\Delta\omega^3} & \frac{11}{6\Delta\omega^3} & -\frac{5}{12\Delta\omega^3} \\ \frac{1}{24\Delta\omega^4} & -\frac{1}{6\Delta\omega^4} & \frac{1}{4\Delta\omega^4} & -\frac{1}{6\Delta\omega^4} & \frac{1}{24\Delta\omega^4} \end{pmatrix} \begin{pmatrix} p_1 + 2q_1\pi \\ p_2 + 2q_2\pi \\ p_3 + 2q_3\pi \\ p_4 + 2q_4\pi \\ p_5 + 2q_5\pi \end{pmatrix} \\
&= \begin{pmatrix} 5(p_1 + 2q_1\pi) - 10(p_2 + 2q_2\pi) + 10(p_3 + 2q_3\pi) - 5(p_4 + 2q_4\pi) + p_5 + 2q_5\pi \\ \frac{1}{12\Delta\omega}\{-77(p_1 + 2q_1\pi) + 214(p_2 + 2q_2\pi) - 234(p_3 + 2q_3\pi) + 122(p_4 + 2q_4\pi) - 25(p_5 + 2q_5\pi)\} \\ \frac{1}{24\Delta\omega^2}\{71(p_1 + 2q_1\pi) - 236(p_2 + 2q_2\pi) + 294(p_3 + 2q_3\pi) - 164(p_4 + 2q_4\pi) + 35(p_5 + 2q_5\pi)\} \\ \frac{1}{12\Delta\omega^3}\{-7(p_1 + 2q_1\pi) + 26(p_2 + 2q_2\pi) - 36(p_3 + 2q_3\pi) + 22(p_4 + 2q_4\pi) - 5(p_5 + 2q_5\pi)\} \\ \frac{1}{24\Delta\omega^4}\{p_1 + 2q_1\pi - 4(p_2 + 2q_2\pi) + 6(p_3 + 2q_3\pi) - 4(p_4 + 2q_4\pi) + p_5 + 2q_5\pi\} \end{pmatrix}.
\end{aligned} \tag{A2b}$$

Arranging the above result, as an example, regarding the second-order dispersion involved in the spectral phase, we have the following equation for $\Psi_2(\Delta\omega)^2$:

$$\begin{aligned}
\psi_2(\Delta\omega)^2 &= \frac{1}{24}\{71(p_1 + 2q_1\pi) - 236(p_2 + 2q_2\pi) + 294(p_3 + 2q_3\pi) - 164(p_4 + 2q_4\pi) + 35(p_5 + 2q_5\pi)\} \\
&= \frac{1}{24}\Big\{2\pi \underbrace{(71q_1 - 2^2\times 59q_2 + 2\times 3\times 7^2 q_3 - 2^2\times 41q_4 + 5\times 7q_5)}_{\mathrm{A}} \\
&\quad + \underbrace{(71p_1 - 2^2\times 59p_2 + 2\times 3\times 7^2 p_3 - 2^2\times 41p_4 + 5\times 7p_5)}_{\mathrm{B}}\Big\}.
\end{aligned} \tag{A3}$$

As q_m takes arbitrary integers, thereby, the term A is (mostly) an arbitrary integer. The term B is a real number determined by the spectral-phase p_m. Here, we rewrite ϕ_2 as $\phi_2 = \mathrm{mod}[\psi_2(\Delta\omega)^2, 2\pi]$, and then obtain

$$\phi_2 = 2\pi\frac{s}{24} + \frac{P_2}{24} \quad (s = 0,1,\ldots,23). \tag{A4}$$

Thus, we find that the second-order dispersion ϕ_2 is reduced to 24 values. Here P_2 is a real number given by $\mathrm{mod}[71p_1 - 2^2\times 59p_2 + 2\times 3\times 7^2 p_3 - 2^2\times 41p_4 + 5\times 7p_5, 2\pi]$.

Similarly, if we arrange the third-order dispersion $\phi_3 = \mathrm{mod}[\psi_3(\Delta\omega)^3, 2\pi]$, we obtain

$$\psi_3(\Delta\omega)^3 = \frac{1}{12}\Big\{2\pi \underbrace{(-7q_1 + 26q_2 - 36q_3 + 22q_4 - 5q_5)}_{C} + \underbrace{(-7p_1 + 26p_2 - 36p_3 + 22p_4 - 5p_5)}_{D}\Big\}. \tag{A5}$$

Namely, the third-order dispersion ϕ_3 is reduced to 12 values:

$$\phi_3 = 2\pi\frac{l}{12} + \frac{P_3}{12} \quad (l = 0,1,\ldots,11). \tag{A6}$$

Here, s and l are restricted to either an even or odd combination (i.e., if s is even, l is even; if s is odd, l is odd). Therefore, $\frac{24\times12}{2} = 144$ solutions—the half of all the combinations of ϕ_2 and ϕ_3—appear with a lattice pattern in the solution space of the second- and third-order dispersions (ϕ_2,ϕ_3).

The reason is as follows: sum of the integer terms A and C is given by

$$\begin{aligned} A + C &= 64q_1 - 210q_2 + 258q_3 - 142q_4 + 30q_5 \\ &= 2(2^5 q_1 - 3\times5\times7q_2 + 3\times43q_3 - 71q_4 + 3\times5q_5). \end{aligned} \tag{A7}$$

Therefore, the sum of A and C is always even. If A is even, C must be even, and if A is odd, C must be odd. As a result, all the solutions allowed in the solution space (ϕ_2,ϕ_3) are reduced to $\frac{24\times12}{2} = 144$. If we repeat the equivalent discussion in another solution space (ϕ_3,ϕ_4), we also find $\frac{12\times24}{2} = 144$ solutions with a lattice pattern in the solution space (ϕ_3,ϕ_4).

If we arrange the term $\Psi_4(\Delta\omega)^4$ as well, we obtain

$$\begin{aligned} \psi_4(\Delta\omega)^4 = \frac{1}{24}\Big\{ & 2\pi \underbrace{(q_1 - 4q_2 + 6q_3 - 4q_4 + q_5)}_{E} \\ & + \underbrace{(p_1 - 4p_2 + 6p_3 - 4p_4 + p_5)}_{F} \Big\}. \end{aligned} \tag{A8}$$

Therefore, the sum of C and E is given by

$$\begin{aligned} C + E &= -6q_1 + 22q_2 - 30q_3 + 18q_4 - 4q_5 \\ &= 2(-3q_1 + 11q_2 - 15q_3 + 9q_4 - 2q_5). \end{aligned} \tag{A9}$$

As a result, all the solutions allowed in the solution space of the third- and fourth-order dispersions, (ϕ_3,ϕ_4), are reduced to $\frac{12\times24}{2} = 144$, as in case of (ϕ_2,ϕ_3).

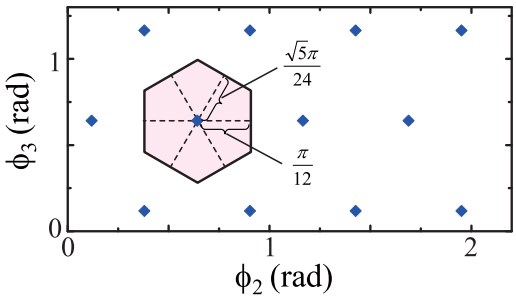

FIG. 5. A unit cell of the solution space (ϕ_2,ϕ_3).

On the other hand, regarding the solution space of the second-and fourth-order dispersions, (ϕ_2,ϕ_4), unlike in the above two examples, $A + E$ is given by

$$\begin{aligned} A + E &= 72q_1 - 240q_2 + 300q_3 - 168q_4 + 36q_5 \\ &= 12(2\times3q_1 - 2^2\times5q_2 + 5^2q_3 - 2\times7q_4 + 3q_5). \end{aligned} \tag{A10}$$

Therefore, the sum of A and E must be a multiple of 12, as a result of which the combinations of A and E are restricted to 12 cases to satisfy it. All the solutions allowed in the solution space of the second- and fourth-order dispersions, (ϕ_2,ϕ_4), are therefore reduced to $\frac{24\times24}{12} = 48$.

To summarize all the above results, $\frac{24\times12\times24}{2\times12} = 288$ solutions in total are distributed with a lattice pattern in the three-dimensional solution space (ϕ_2,ϕ_3,ϕ_4) of the second-, third-, and fourth-order dispersions.

Figure 5 is an example in which the solutions (blue diamonds) appear with a lattice pattern in the solution space (ϕ_2,ϕ_3). The hexagonal zone represents one unit cell of the solution space. That is, if the target spectral-phase $\phi(\omega_m)$ is different, the lattice pattern, as a whole, translationally moves in the solution space (ϕ_2,ϕ_3), where the hexagonal zone is the meaningful shiftable area, as the pattern is reciprocal.

[1] C. Froehly, B. Colombeau, and M. Vampouille, Shaping and analysis of picosecond light pulses, in *Progress in Optics*, edited by E. Wolf (Elsevier, North-Holland, Amsterdam, 1983), Vol. 20, pp. 63–153.

[2] A. M. Weiner, Femtosecond pulse shaping using spatial light modulators, Rev. Sci. Instrum. **71**, 1929 (2000).

[3] N. K. Fontaine, R. P. Scott, L. Zhou, F. M. Soares, J. P. Heritage, and S. J. B. Yoo, Real-time full-field arbitrary optical waveform measurement, Nat. Photon. **4**, 248 (2010).

[4] K. Takiguchi, K. Okamoto, I. Kominato, H. Takahashi, and T. Shibata, Flexible pulse waveform generation using silica-waveguide-based spectrum synthesis circuit, Electron. Lett. **40**, 537 (2004).

[5] S. T. Cundiff and A. M. Weiner, Optical arbitrary waveform generation, Nat. Photon. **4**, 760 (2010).

[6] A. V. Sokolov, D. R. Walker, D. D. Yavuz, G. Y. Yin, and S. E. Harris, Femtosecond Light Source for Phase-Controlled Multiphoton Ionization, Phys. Rev. Lett. **87**, 033402 (2001).

[7] K. R. Pandiri, T. Suzuki, A. Suda, K. Midorikawa, and M. Katsuragawa, Line-by-line control of 10-THz-frequency-spacing Raman sidebands, Opt. Express **18**, 732 (2010).

[8] K. R. Pandiri and M. Katsuragawa, A 10 THz ultrafast function generator-generation of rectangular and triangular pulse trains, New J. Phys. **13**, 023030 (2011).

[9] H.-S. Chan, Z.-M. Hsieh, W.-H. Liang, A. H. Kung, C.-K. Lee, C.-J. Lai, R.-P. Pan, and L.-H. Peng, Synthesis and measurement of ultrafast waveforms from five discrete optical harmonics, Science **331**, 1165 (2011).

[10] Th. Udem, J. Reichert, R. Holzwarth, and T. W. Hänsch, Absolute Optical Frequency Measurement of the Cesium D1 Line with a Mode-Locked Laser, Phys. Rev. Lett. **82**, 3568 (1999).

[11] D. J. Jones, S. A. Diddams, J. K. Ranka, A. Stentz, R. S. Windeler, J. L. Hall, and S. T. Cundiff, Carrier-envelope phase control of femtosecond mode-locked lasers and direct optical frequency synthesis, Science **288**, 635 (2000).

[12] E. Goulielmakis, M. Uiberacker, R. Kienberger, A. Baltuska, V. Yakovlev, A. Scrinzi, Th. Westerwalbesloh, U. Kleineberg, U. Heinzmann, M. Drescher, and F. Krausz, Direct measurement of light waves, Science **305**, 1267 (2004).

[13] A. Wirth, M. Th. Hassan, I. Grguraš, J. Gagnon, A. Moulet, T. T. Luu, S. Pabst, R. Santra, Z. A. Alahmed, A. M. Azzeer,

V. S. Yakovlev, V. Pervak, F. Krausz, and E. Goulielmakis, Synthesized light transients, Science **334**, 195 (2011).

[14] M. Shapiro and P. Brumer, Coherent control of molecular dynamics, Rep. Prog. Phys. **66**, 859 (2003).

[15] C. Brif, R. Chakrabarti, and H. Rabitz, Control of quantum phenomena: Past, present and future, New J. Phys. **12**, 075008 (2010).

[16] R. Bartels, S. Backus, E. Zeek, L. Misoguti, G. Vdovin, I. P. Christov, M. M. Murnane, and H. C. Kapteyn, Shaped-pulse optimization of coherent emission of high-harmonic soft x-ray, Nature (London) **406**, 164 (2000).

[17] A. Schiffrin, T. P. Colberg, N. Karpowicz, V. Apalkov, D. Gerster, S. Mühlbrandt, M. Korbman, J. Reichert, M. Schultze, S. Holzner, J. V. Barth, R. Kienberger, R. Ernstorfer, V. S. Yakovlev, M. I. Stockman, and F. Krausz, Optical-field-induced current in dielectrics, Nature (London) **493**, 70 (2013).

[18] M. Schultze, E. M. Bothschafter, A. Sommer, S. Holzner, W. Schweinberger, M. Fiess, M. Hofstetter, R. Kienberger, V. Apalkov, V. S. Yakovlev, M. I. Stockman, and F. Krausz, Controlling dielectrics with the electric field of light, Nature (London) **493**, 75 (2013).

[19] N. S. Suhaimi, C. Ohae, T. Gavara, K. Nakagawa, F.-L. Hong, and M. Katsuragawa, Generation of phase-locked five harmonics by implementing an optical frequency division technology, Opt. Lett. **40**, 5802 (2015).

[20] G. Ghosh, Dispersion-equation coefficients for the refractive index and birefringence of calcite and quartz crystals, Opt. Commun. **163**, 95 (1999).

[21] M. J. Dodge, Refractive properties of magnesium fluoride, Appl. Optics **23**, 1980 (1984).

[22] M. A. Schumer and K. Steiglitz, Adaptive step size random search, IEEE Trans. Automat. Contr. **13**, 270 (1968).

[23] I. H. Malitson, Interspecimen comparison of the refractive index of fused silica, J. Opt. Soc. Am. **55**, 1205 (1965).

[24] M. Katsuragwa, K. Yokoyama, T. Onose, and K. Misawa, Generation of a 10.6-THz ultrahigh-repetition-rate train by synthesizing phase-coherent Raman-sidebands, Opt. Express **13**, 5628 (2005).

[25] T. Suzuki and M. Katsuragawa, Femtosecond ultrashort pulse generation by addition of positive material dispersion, Opt. Express **18**, 23088 (2010).

[26] T. Jannson and J. Jannson, Temporal self-imaging effect in single-mode fibers, J. Opt. Soc. Am. **71**, 1373 (1981).

[27] J. Fatome, S. Pitois, and G. Millot, Influence of third-order dispersion on the temporal Talbot effect, Opt. Commun. **234**, 29 (2004).

[28] K. Yoshii, J. K. Anthony, and M. Katsuragawa, The simplest route to generating a train of attosecond pulses, Light: Sci. App. **2**, e58 (2013).

[29] Correlation coefficient: $\frac{\int_{-\tau/2}^{\tau/2} E_{\mathrm{Target}}(t) E_{\mathrm{Explored}}(t) dt}{\sqrt{\int_{-\tau/2}^{\tau/2} E_{\mathrm{Target}}(t)^2 dt} \sqrt{\int_{-\tau/2}^{\tau/2} E_{\mathrm{Explored}}(t)^2 dt}}$

[30] M. Nomura, Arbitrary polarization manipulation of a set of highly discrete coherent spectra, Master's thesis, University of Electro-Communications, Tokyo, Japan (2016).

[31] M. Sato, T. Higuchi, N. Kanda, K. Konishi, K. Yoshioka, T. Suzuki, K. Misawa, and M. Kuwata-Gonokami, Terahertz polarization pulse shaping with arbitrary field control, Nat. Photon. **7**, 724 (2013).

[32] K. Yoshii, Y. Nakamura, K. Hagihara, and M. Katsuragawa, Generation of a train of ultrashort pulses by simply inserting transparent plates on the optical path, *Conference on Lasers and Electro-Optics/Quantum Electronics and Laser Science (CLEO/QELS) 2014*, OSA Technical Digest (online) (Optical Society of America, 2014), paper FTh1D.5.

[33] S. E. Harris and A. V. Sokolov, Broadband spectral generation with refractive index control, Phys. Rev. A **55**, R4019 (1997).

[34] A. V. Sokolov, D. R. Walker, D. D. Yavuz, G. Y. Yin, and S. E. Harris, Raman Generation by Phased and Antiphased Molecular States, Phys. Rev. Lett. **85**, 562 (2000).

[35] J. Q. Liang, M. Katsuragawa, F. Le Kien, and K. Hakuta, Sideband Generation using Strongly Driven Raman Coherence in Solid Hydrogen, Phys. Rev. Lett. **85**, 2474 (2000).

[36] F. Couny, F. Benabid, P. J. Roberts, P. S. Light, and M. G. Raymer, Generation and photonic guidance of multi-octave optical-frequency combs, Science **318**, 1118 (2007).

[37] F. Belli, A. Abdolvand, W. Chang, J. C. Travers, and P. St. J. Russell, Vacuum-UV to IR supercontinuum in hydrogen-filled photonic crystal fiber, Optica **2**, 292 (2015).

[38] M. Krüger, M. Schenk, and P. Hommelhoff, Attosecond control of electrons emitted from a nanoscale metal tip, Nature (London) **475**, 78 (2011).

[39] K. Yoshioka, I. Katayama, Y. Minami, M. Kitajima, S. Yoshida, H. Shigekawa, and J. Takeda, Real-space coherent manipulation of electrons in a single tunnel junction by single-cycle terahertz electric fields, Nat. Photon. **10**, 762 (2016).

[40] J. Zheng and M. Katsuragawa, Freely designable optical frequency conversion in Raman-resonant four-wave-mixing process, Sci. Rep. **5**, 8874 (2015).